Multi-scale finite element modeling of 3D printed structures subjected to mechanical loads

Dalia Calneryte and Rimantas Barauskas
Department of Applied Informatics, Kaunas University of Technology, Kaunas, Lithuania
Daiva Milasiene
Department of Materials Engineering, Kaunas University of Technology, Kaunas, Lithuania
Rytis Maskeliunas
Department of Multimedia Engineering, Kaunas University of Technology, Kaunas, Lithuania
Audrius Neciunas
Department of Applied Informatics, Kaunas University of Technology, Kaunas, Lithuania
Armantas Ostreika
Department of Multimedia Engineering, Kaunas University of Technology, Kaunas, Lithuania, and
Martynas Patasius and Andrius Krisciunas
Department of Applied Informatics, Kaunas University of Technology, Kaunas, Lithuania

Abstract

Purpose – The purpose of this paper is to investigate the influence of geometrical microstructure of items obtained by applying a three-dimensional (3D) printing technology on their mechanical strength.

Design/methodology/approach – Three-dimensional printed items (3DPI) are composite structures of complex internal constitution. The buildup of the finite element (FE) computational models of 3DPI is based on a multi-scale approach. At the micro-scale, the FE models of representative volume elements corresponding to different additive layer heights and different thicknesses of extruded fibers are investigated to obtain the equivalent non-linear nominal stress–strain curves. The obtained results are used for the creation of macro-scale FE models, which enable to simulate the overall structural response of 3D printed samples subjected to tensile and bending loads.

Findings – The validation of the models was performed by comparing the computed results against the experimental ones, where satisfactory agreement has been demonstrated within a marked range of thicknesses of additive layers. Certain inadequacies between computed against experimental results were observed in cases of thinnest and thickest additive layers. The principle explanation of the reasons of inadequacies takes into account the poorer quality of mutual adhesion in case of very thin extruded fibers and too-early solidification effect.

Originality/value – Flexural and tensile experiments are simulated by FE models that are created with consideration to microstructure of 3D printed samples.

Keywords Finite elements, 3D printed items, Multi-scale modelling, Strength analysis

Paper type Research paper

1. Introduction

Additive manufacturing (Su *et al.*, 2007) technology offers many advantages if compared against traditional manufacturing, such as easy implementation of geometrically complex designs, low material cost and little material waste. Multiple materials or colors may be easily combined within the same manufactured item (Atzeni *et al.*, 2010). Certain disadvantages can be mentioned, such as poor appearance of the surface finish compared to molded items, as well as the necessity to use constitutive materials with low melting point (Groza and Shackelford, 2010). However, open source three-dimensional (3D) printers enable the practical implementation of complex designs in the public domain and, in this way, promote the sustainable development (Jones *et al.*, 2011; Holland *et al.*, 2010; Pearce *et al.*, 2010; Kentzer *et al.*, 2011).

Predictions of the mechanical strength of 3D printed items (3DPI) are highly important in case the printed details are used in real operational mechanical assemblies. The final strength of the printed product is determined by the combined effect of material properties and the micro-geometry of the pattern of

The current issue and full text archive of this journal is available on Emerald Insight at: **www.emeraldinsight.com/1355-2546.htm**

Rapid Prototyping Journal
24/1 (2018) 177–187
 [ISSN 1355-2546]
[DOI 10.1108/RPJ-05-2016-0074]

Received 5 May 2016
Revised 13 October 2016
7 February 2017
Accepted 14 March 2017

strings extruded as the nozzle of the 3D printer moves along the path prescribed by the item design. The material properties of the string can be measured by applying certain standard procedures (Groza and Shackelford, 2010). Research (Lee *et al.*, 2007; Bellini and Güçeri, 2003) characterizes the process parameters such as raster orientation, air gap, bead width, color and temperatures schemes used during the fused deposition modeling (FDM), and Lee *et al.* (2007) demonstrates that string directions and raster angles are important parameters determining the final compressive strength.

From the point of view of mechanics of materials, the 3DPI are composite structures of complex internal constitution. At macro-scale, the models of 3DPI may be developed by assuming their internal constitution as orthotropic continua. Experimental tensile tests were performed to determine nine mechanical constants defining the averaged orthotropic stiffness tensor (Domingo-Espin *et al.*, 2015). The dynamic properties of ABS thermoplastic material have been investigated in Arivazhagan and Masood (2012), Jami *et al.* (2013) and Thrimurthulu *et al.* (2004). Research (Tymrak *et al.*, 2014) demonstrated that parts printed from tuned, low-cost, open-source printers can achieve similar qualities as those obtained from commercial vendors. Anisotropic and brittle nature of 3DPI makes it important to analyze the effect of process parameters to the resistance to compressive loading for enhancing service life of functional parts (Sood *et al.*, 2012). The influence of layer thickness, orientation, raster angle, raster width and air gap are considered in Sood *et al.* (2010). The influence of layer filling type on part capability of carrying loads and economical coefficients of the manufacturing process was analyzed in Gorski *et al.* (2014) with application to ABS thermoplastic. The evaluation of profile errors and extruding apertures is presented in Chang and Huang (2011). Effect of material color (PLA plastic) on the properties of the 3DPI was considered in Wittbrodt and Pearce (2015). The results demonstrated a marked relationship between the tensile strength and per cent crystallinity of a printed sample and a marked relationship between per cent crystallinity and the temperature of the extruder nozzle. The elastic moduli and mechanical strength values of ABS thermoplastic were determined for the ABS monofilament feedstock and for various unidirectional FD-ABS materials in Rodríguez *et al.* (2003). Properties of tensile strength of ABS parts were analyzed in Ahn *et al.* (2002) comparing results against the injection molded ABS parts. The properties of vibrations of 3DPI were analyzed in Chaitanya *et al.* (2015).

The purpose of this paper is to investigate the influence of geometrical microstructure on mechanical properties of the structures manufactured using additive technology. In this study, we determine the influence of additive layers heights and of the thickness of extruded strings on the strength of the 3D printed structure by using the multi-scale modeling techniques. Two-scale sequential approach was applied. FE models of representative volume elements (RVE) corresponding to various additive layer heights and fiber thicknesses were analyzed at a micro-scale by using implicit analysis to determine nominal stress–strain curves. The obtained parameters were applied for macro-scale FE models by assuming the material properties as homogeneous orthotropic. Computational and physical tensile and three-point flexural tests on the 3D printed samples were performed. Numerical simulations were performed by using FE program LS-DYNA. The comparison of the results enabled to validate the unknown values of material parameters and allowed to choose appropriate layer thickness for the items manufactured using additive technology and evaluate whether simulation results correspond the behavior of the real item.

2. Evaluation of material properties using RVE

2.1 Micro-scale finite element models

A structure printed by 3DP is a composite structure of complex geometrical microstructure containing air gaps, as well as intersections between fibers in the adjacent layers and fibers in the same layer. In case of parallel fibers, the printed structure can be regarded as a unidirectional composite material.

The idealized situation is considered in this research by assuming the representative volume element (RVE) as a small periodical cell covering all heterogeneities of the internal structure corresponding to different layer height. The RVEs are designed after the analysis of GCode generated by slicing software Slic3r, which predetermines the movement of the printer nozzle. Each RVE consists of one full fiber surrounded by half of adjacent inter- and intra-layer fibers. RVEs of structures of different layer thicknesses are of different geometrical sizes as the same volume of the extruded material is spread wider in case of thinner layers. The cross-section of the fiber is approximated as a rounded rectangular (Figure 1). The distance between the centerlines of adjacent fibers in the same layer is equal to the shift of the 3DP nozzle in transverse direction to the next parallel fiber. To imitate the bonding between layers and between fibers in the same layer, the diameters of the circles are assumed to be equal to the layer thickness increased by 20 per cent. The increment value was chosen so that the extruded volume of the fiber according to the GCode and calculated using the cross-section of the rounded rectangular with overlap taken into account (gray area in Figure 1) differ less than 5 per cent for the specimen used for the tensile and flexure tests with longitudinal and transverse printing directions. The micromodels of RVEs were meshed by using the ANSYS meshing tool with four-noded tetrahedron elements (Figure 2).

In this research, we investigated the influence of the characteristic geometrical features of the extruded micro-structure of 3DPIs on the mechanical strength defined as limit stress. The LS-DYNA *MAT_PLASTIC_KINEMATIC

Figure 1 The geometry of the cross-section of nine parallel fibers in micro-scale (h_l– layer thickness, d – distance between centers of adjacent fibers)

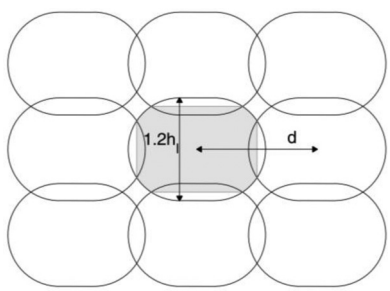

Figure 2 Representative volume elements used in micro-scale of various layer thicknesses $h_l = 0.2\ mm$ (a), $h_l = 0.25\ mm$ (b), $h_l = 0.3\ mm$ (c), $h_l = 0.35\ mm$ (d), $h_l = 0.4\ mm$ (e)

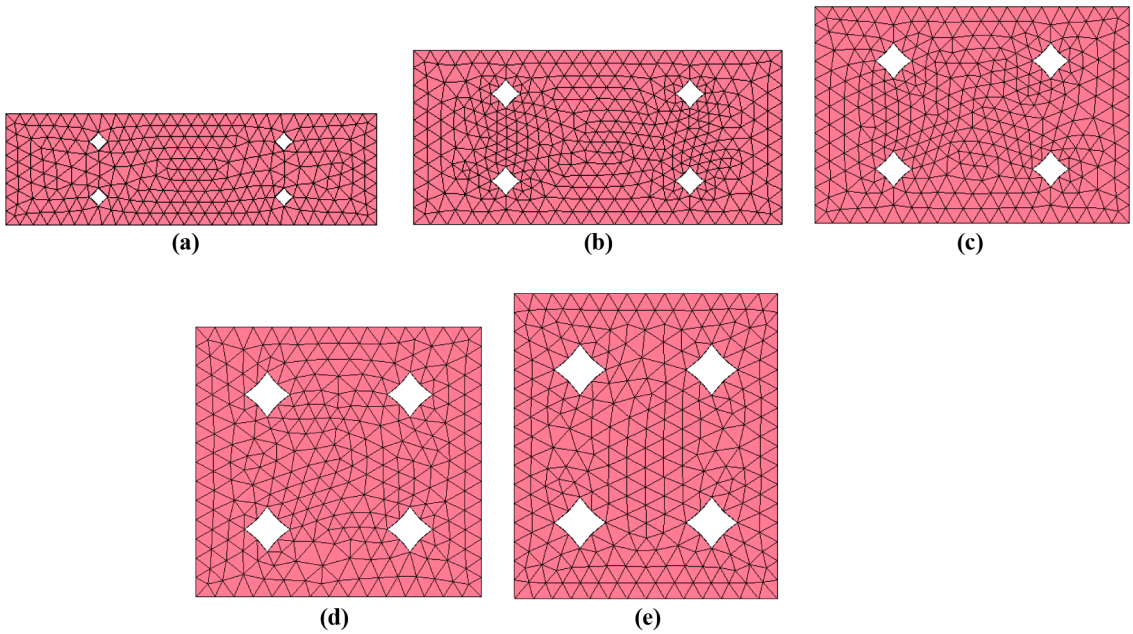

material model was applied for FE models of constant stress solid elements in micro-scale with parameters listed in Table I and the effective stress–strain curve in Figure 3. This material model enables to define failure strain for eroding elements in finite strains simulations.

2.2 Stress–strain curves of material model in macro-scale

The 3DPI is considered as a unidirectional composite in case the material is fused in parallel lines. The unidirectional composite is modeled as orthotropic homogeneous material in the macro-scale with principal axis along the fibers, transverse to the fibers of the same layer and augmentation direction. In the macro scale, the orthotropic internal micro-structure of 3DPI is presented by material model *MAT_NONLINEAR_ORTHOTROPIC applied for solid. The material model in small strains range is defined by the linear stiffness tensor. At finite strains, the non-linear behavior of the material is described by nominal stress versus strain curves in three perpendicular directions, such as fiber direction, transverse intra-layer direction (perpendicular to parallel fibers within a layer) and inter-layer direction (perpendicular to parallel adjacent layers). The strains are calculated as $\lambda - 1$, where λ is the stretch ratio along the corresponding direction. The shear behavior is defined by nominal shear versus strain curves in three orthogonal material planes. The shear strain is defined as $\sin(\gamma)$ with shear angle γ.

Table I Material parameters of the micro-scale model

Young's modulus, N/m^2	2.9E+009
Poisson's ratio	0.32
Yield stress, N/m^2	3E+007
Tangent modulus, N/m^2	5e8
Failure strain for eroding elements	0.07

Figure 3 The effective stress–strain curve of the material used in micro-scale

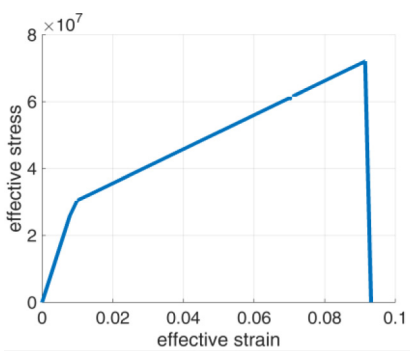

The effective stiffness tensor is obtained by using by micro-mechanical analysis of RVE (Calneryte and Barauskas, 2016). The strain states of the RVE representing three pure uni-axial and three pure shear strain states are determined by prescribing displacements of the nodes of boundary surfaces. The resulting stresses are multi-axial in all six cases. The matrices containing strains and averaged stresses represent each loading case and are applied to calculate effective stiffness tensor. Generally, the same effective tensor could be obtained if strain and stress matrices were formed by creating six independent multi-axial states of RVE with corresponding average stresses. In this research, the approach was extended to determine non-linear stress–strain relationship of the material.

The micro-models defined in Figure 2 were loaded by prescribed displacements in accordance with the boundary conditions representing pure uni-axial strain (1-3) and pure

shear (4-6) states of RVE positioned in the origin of coordinate system (Figure 4):

$$I: \quad u_x(a,y,z)=\delta, u_x(0,y,z)=0, \quad u_y(x,0,z)=u_y(x,b,z)=0, \quad u_z(x,y,0)=u_z(x,y,c)=0 \tag{1}$$

$$II: \quad u_x(0,y,z)=u_x(a,y,z)=0, \quad u_y(x,b,z)=\delta, u_y(x,0,z)=0, \quad u_z(x,y,0)=u_z(x,y,c)=0 \tag{2}$$

$$III: \quad u_x(0,y,z)=u_x(a,y,z)=0, \quad u_y(x,0,z)=u_y(x,b,z)=0, \quad u_z(x,y,c)=\delta, u_z(x,y,0)=0 \tag{3}$$

$$IV: \quad u_x(x,b,z)=\delta, u_x(0,y,z)=u_x(a,y,z), \quad u_y(a,y,z)=\delta, u_y(x,0,z)=u_y(x,b,z), \quad u_z(x,y,0)=u_z(x,y,c)=0 \tag{4}$$

$$V: \quad u_x(0,y,z)=u_x(a,y,z)=0, \quad u_y(x,y,c)=\delta, u_y(x,0,z)=u_y(x,b,z), \quad u_z(x,b,z)=\delta, u_z(x,y,0)=u_z(x,y,c) \tag{5}$$

$$VI: \quad u_x(x,y,c)=\delta, u_x(0,y,z)=u_x(a,y,z), \quad u_y(a,0,z)=u_y(x,b,z)=0, \quad u_z(a,y,z)=\delta, u_z(x,y,0)=u_z(x,y,c) \tag{6}$$

where $u_x(x, y, z)$, $u_y(x, y, z)$, $u_z(x, y, z)$ are displacements in X, Y, Z directions correspondingly and a, b and c are length, width and height of RVE. Experimental tests were performed at low strain rate; therefore, no dynamic effects were considered. To avoid dynamic effects, the quasi-static implicit FE analysis of micro-models was applied to determine stress–strain relationships.

The effective non-linear stress–strain curves were calculated from the RVE micro-model by applying the finite linearly increasing displacements on the boundary surfaces in accordance with the scheme in Figure 3. Each loading case creates one uni-axial strain or pure shear strain condition and provides the relationship of the stress component in the direction of the strain averaged over the volume of RVE (Figure 5). This characteristic is necessary for defining the material model *MAT_NONLINEAR_ORTHOTROPIC.

The calculated stress–strain relationships, as well as failure parameters depend on the volume filling. RVE of the thinnest layer height provides highest uniaxial strength and strain values. However, the inter-layer shear strength (XY plane) is higher for the structures with thicker layers. Similarly, the highest shear strength in YZ plane is for the structure with layer thickness of 0.35 *mm* where the fiber cross-sections are almost circular. For the ZX shear stress versus strain curves, the highest strength is reached for the model with 0.3 *mm* layer height. The maximum point of the stress curve is reached at higher strain value for the models with thinner layers.

3. Manufacture of specimens

Two major groups of specimens were produced. One group for tensile test (a rectangular parallelepiped) and other for flexure test (*ISO 178*). Flexure test sample group was divided into two subgroups in accordance with the direction of the fibers in a layer. Two types of structure were considered, where fibers filled the microstructure layer by layer in longitudinal or transverse directions (Figure 6). To analyze influence of layer height, all types of specimen were manufactured for the internal structures with five different layer heights (0.2, 0.25, 0.3, 0.35, 0.4 *mm*). In all, five samples were printed for each type (tensile, flexure longitudinal printing direction, flexure transverse printing direction)/layer height configuration. However, two

Figure 4 Schemes for creating pure strains: I – longitudinal strain mode; II, III – transverse strain modes; IV, V, VI – shear strain modes in XY, YZ, ZX planes respectively

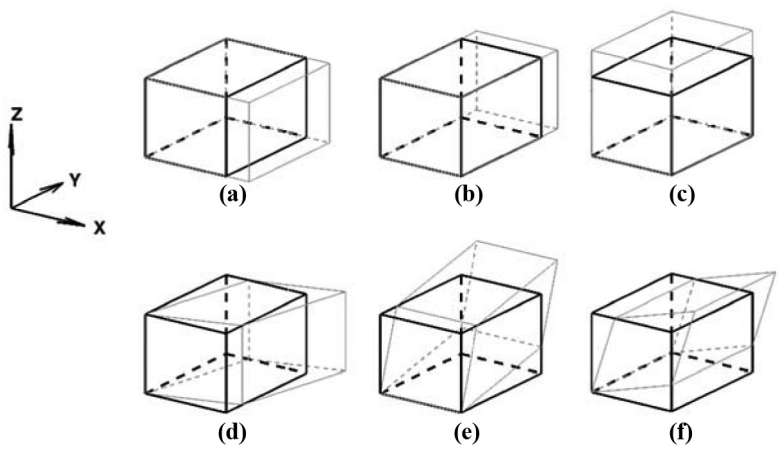

Figure 5 Nominal stress – strain curves (longitudinal (a), transverse along Y and Z axis (b, c), shear in XY (d), YZ (e) and ZX (f) planes) applied in macro-scale for solid elements with *MAT_NONLINEAR_ORTHOTROPIC material model

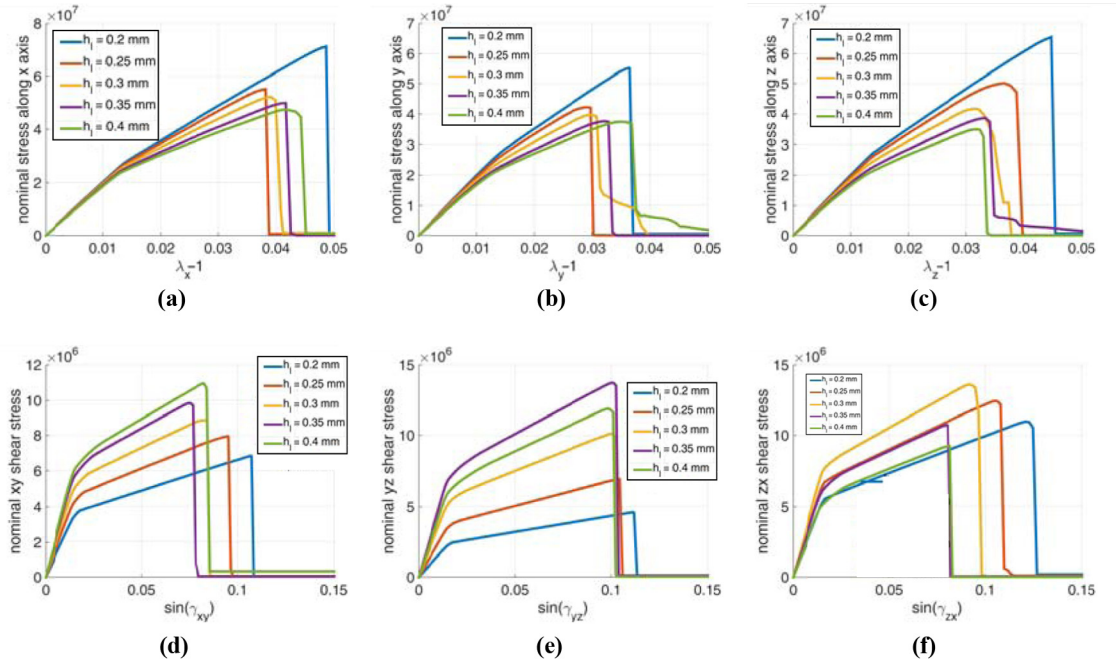

Figure 6 3D printing preview of the sample with longitudinal (a) and transverse (b) printing fibers

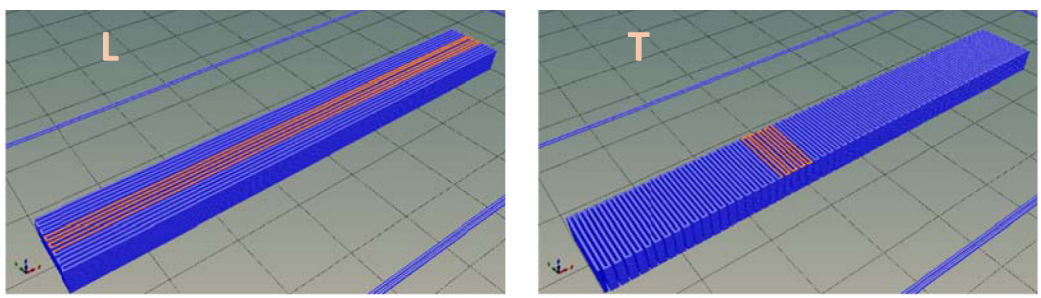

specimens of the tensile group with layer height of 0.4 *mm* were damaged during the experiments and could not be used in the analysis. Both transverse and longitudinal direction samples were used for flexure test, while only samples with fibers of longitudinal direction were subjected to tensile test.

Widely used material PLA (polylactic acid) was chosen for samples. The specimens were printed by *Prusa i3* 3DP. The movements of the print head are governed by GCode generated by using the slicing software that converts digital 3D model to the head movement instructions and sets up the parameters such as the nozzle temperature, printing speed, extrusion rate, etc. The unidirectional fiber model was selected to facilitate the identification of the elasticity parameters by using multi-scale FE modeling. However, traditional slicing software generates the rectilinear filling pattern of perpendicular fibers in adjacent layers. To print a completely unidirectional specimen, the GCode generated by slicing software Slic3r was modified. First, the 3D sample form was converted to GCode. The first layer fibers are printed at a slower movement rate of the head than the other layers to improve the adhesion between the material and the bed. Moreover, this layer includes movement instructions for additional structures like the skirt line which is printed to start the material flow. Therefore, this part of the original GCode for printing the first layer was included in the modified GCode. The GCode for samples with longitudinal printing direction was obtained after modifying the GCode generated with 0° filling angle. Modified GCode generated with 90° filling angle was used to print samples with transverse printing direction. The filling density of each specimen was 100 per cent, and no outlines were needed to maintain the shape of printed object, as the voids along the outline–infill boundary obscure the effect of print orientation (Melenka *et al.*, 2015). Finally, the new GCode was appended by replicating the third layer with the uplift in the printing direction of magnitude equal to the layer thickness to form the structure that satisfies the dimensions of specimen. The cooling and solidification rate of

the extruded plastic is governed by the cooling fan. The geometry of samples does not include cases where quick solidification is required like thin walls, overhangs or bridges. Thus, the cooling fan was disabled during the printing process. Other parameters used for printing process are presented in Table II. As layer heights of each specimen group differ, the quantity of layers varies from 10 for specimen with 0.4 *mm* layer height to 20 for specimen with 0.2 *mm* layer height. Moreover, the overall height of the specimen may slightly vary because the height of the standard specimen divided by layer height has a quotient that is not the whole number and the quotient rounded to the next lowest integer is a number of layers in specimen.

4. Numerical and experimental results

Experimental tension and three-point bending tests were carried out for samples described in Section 2 by using the testing machine *TINIUS Olsen H25KT*. The output parameters of the tests were force (*N*) and displacement (*mm*). The overall thickness and width of each specimen were measured at three points. The mean values were applied to calculate the value of stress $\overline{\sigma}$ in tensile test and $\hat{\sigma}$ in three-point bending test as:

$$\overline{\sigma} = \frac{F}{b \cdot h} \tag{7}$$

$$\hat{\sigma} = \frac{3 \cdot F \cdot Ls}{2 \cdot b \cdot h^2} \tag{8}$$

where b and h are width and height of the specimen, respectively; Ls is a span length between the supporting cylinders; F is a force added to deform the 3DPI.

The experimental results of the group of specimens with the same layer height are represented by the typical $\overline{\sigma}$ versus displacement curve which was identified from the curves of the group by means of the least square method. Then the typical curve was compared with the results of numerical simulations for the model with the stress versus strain curves corresponding to the micro-model with the layer thickness of the group.

Material model *MAT_NONLINEAR_ORTHOTROPIC is applied for eight-noded hexahedron constant stress solid elements in macro-scale FE models. The material direction is defined for each FE individually by using *ELEMENT_SOLID_ORTHO element type in LS-DYNA. Although the fibers in the real printed structure are not unidirectional near the boundaries where 3DP nozzle moves to the adjacent parallel fiber, the U-turns are not considered in the macro model. This results in a simpler macro-model with uniform material properties for all solid elements.

Table II Printing process parameters

Print speed	80 mm/s
Print speed for the first layer	30 mm/s
Extruder temperature	200°C
Bed temperature	55°C
Filament diameter	1.75 mm
Extrusion multiplier	1

4.1 Tensile test

The tensile properties of plastics and plastic composites are determined in accordance with the standard ISO 527. However, stress concentrations because of circumference of rectilinear segments may cause premature failure (Ahn *et al.*, 2002). Therefore, a rectangular parallelepiped *150 × 10 × 4 mm* was used in tensile experiments at elongation rate of 50 *mm/min*.

The solid FE model was designed for the simulation of the quasi-static tensile test. The model of dimensions L = 80 *mm*, b = 10 *mm* and h = 4 *mm* defines the section between the two grips of the testing machine. The printed fibers are directed along the length of the specimen (Direction O_x). The constraints are applied only on the ends of the section (Figure 7) to simulate the fixation created by grips. The boundary conditions for the section that is placed in the origin of the coordinates are defined:

$$\begin{gathered} u_x(0,y,z) = 0, \quad v_x(L,y,z) = 50 \ mm/min, \\ u_y(0,0,z) = u_y(0,b,z) = u_y(L,0,z) = u_y(L,b,z) = 0, \\ u_z(0,y,0) = u_z(0,y,h) = u_z(L,y,0) = u_z(L,y,h) = 0, \end{gathered} \tag{9}$$

where $u_x(x, y, z)$, $u_y(x, y, z)$ and $u_z(x, y, z)$, denote displacements in X, Y and Z directions and $v_x(x, y, z)$ denotes the velocity in O_x direction.

At low elongation rate of 50 *mm/min*, no dynamic effects were taken into account. This enabled to perform a quasi-static implicit analysis with increasing load. The force value F used in determining parameter $\overline{\sigma}$ was obtained at the middle cross-section of the specimen perpendicular to the loading direction.

The numerical results [Figure 8(a)] show that the maximum $\overline{\sigma}(\overline{\sigma}_{max})$ value was reached by the specimen with parameters calculated for the micro-model with thinnest layer and $\overline{\sigma}(\overline{\sigma}_{max})$ values decrease for the models corresponding to the thicker layers. Numerical simulations for the models corresponding to layer heights 0.2 *mm*, 0.25 *mm* and 0.3 *mm* were stopped because of instabilities in the model that are the result of a steep fall in of the input curves of the material model. If it is assumed that model reached its $\overline{\sigma}_{max}$ before instabilities occur, then the model corresponding to the thicker layer reached its $\overline{\sigma}_{max}$ at lower extension values. Although numerical simulations [Figure 8(a)] imply that the structure with the thinnest layer has highest $\overline{\sigma}_{max}$ values, the highest experimental $\overline{\sigma}_{max}$ was reached for the specimen group with 0.25 *mm* layer thickness [Figure 8(b)]. Nonetheless, the highest extension value at the $\overline{\sigma}_{max}$ value was observed for the sample with the thinnest layer. However, the $\overline{\sigma}_{max}$ values differed less than 5 per cent from the mean value with the exception of the samples with the thickest layer where the lowest $\overline{\sigma}_{max}$ value appeared. In addition, the deviation of results for specimens in the group with the thickest layer was significantly higher than in other groups. This was caused by the facts that the material is fused at higher rate and the adhesion of fibers in adjacent layers and in the same layer is poor.

Difference between numerical and experimental $\overline{\sigma}_{max}$ and extension values at those points did not exceed 10 per cent with the exception of model corresponding to layer height of 0.2 *mm*. In this case, the difference between experimental and simulated $\overline{\sigma}_{max}$ values was more than 40 per cent; the extension values at $\overline{\sigma}_{max}$ differed more than 10 per cent. At the extension

Figure 7 Finite element model for the tensile test (u_x, u_y and u_z represent displacements of the respective boundary or face and v_x represents velocity of the face)

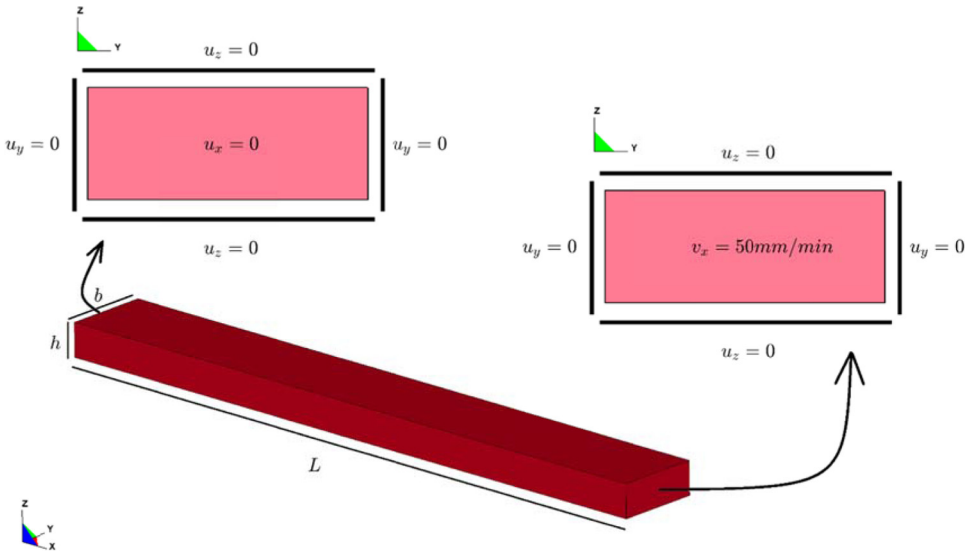

Figure 8 Typical $\overline{\sigma}$ versus extension curves of numerical simulations (a) and experiments (b) of tensile test with $\overline{\sigma}_{max}$ values marked for each curve

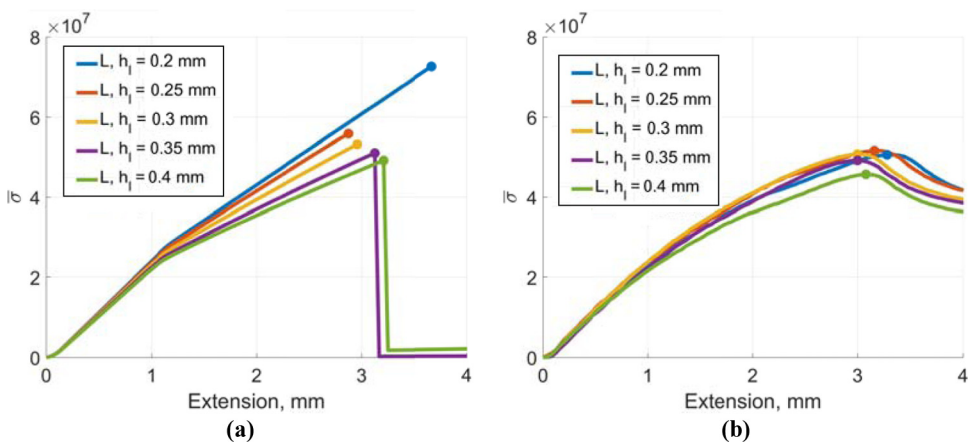

of 1 *mm*, the differences between experimental and respective numerical curves do not exceed 5 per cent. At the extension of 2 *mm*, the tendency is sustained with the exception of the model corresponding to the thinnest layer height. However, in this case, the difference also does not exceed 10 per cent.

The tension test is governed by the fibers and behavior of the numerical model is similar to the input stress–strain curve obtained from the RVE in the fiber direction. As the material model used in the RVE analysis is a rough approximation of PLA stress–strain relations, it was not possible to reproduce the behavior after the maximum point is reached.

The cross-sections of tensile test samples with layer thickness of 0.25 and 0.4 *mm* after the break are shown in Figure 9.

Figure 9 Cross-section of specimens with layer thickness 0.25 *mm* (a) and 0.4 *mm* (b) after the tension test

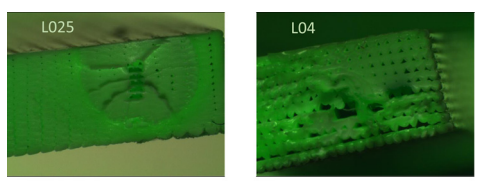

4.2 Three-point flexural test

The three-point flexural test was used to determine the bending stiffness of the structure. The samples for three-point bending test were made in accordance with standard *ISO 178* type. The scheme of flexure experiment is presented in Figure 10 with maximum transverse deflection of 18 *mm* fixed. The specimen was placed on the supports with the orientation of the last printed layer on top during experiments.

The macro-scale solid FE model of the specimen was constrained by the supporting cylinders of span length Ls = 63 *mm* and the bending cylinder at the center of the specimen.

Figure 10 Finite element model for three point bending (flexure) test

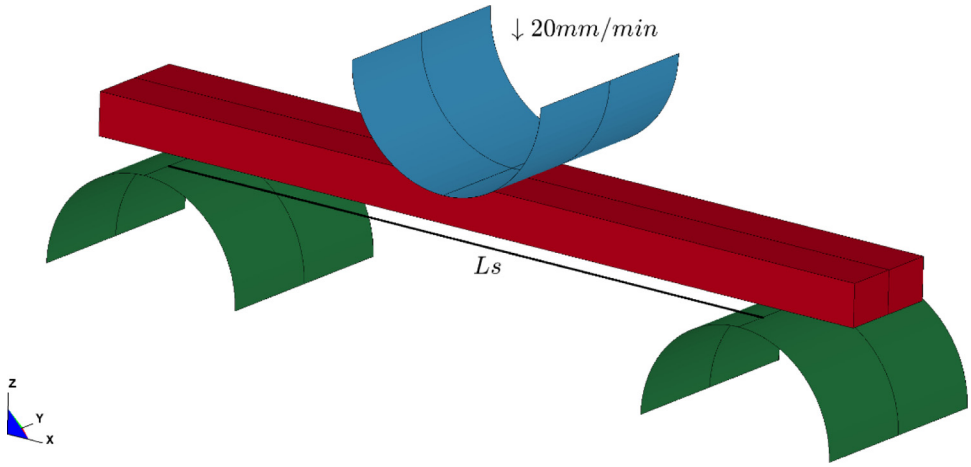

The dimensions of the specimen are $L = 80$ *mm*, $b = 10$ *mm* and $h = 4$ *mm* (Figure 10). Half of model was simulated because of the symmetry conditions. Supporting and bending cylinders were composed of rigid shell elements (*MAT_RIGID) with the thickness of 1 *mm*. The radius of cylinder is 5 *mm*. The top cylinder bended the solid structure at low displacement rate of 20 *mm*/*min*; therefore, no dynamic effects were observed and quasi-static implicit analysis was used in LS-DYNA simulations. The contact type between the cylinders and solid model was *CONTACT_AUTOMATIC_SURFACE_TO_SURFACE. The magnitude of force applied to move the bending cylinder at a given speed was used for evaluation of parameter $\hat{\sigma}$. Bending tests were performed for unidirectional specimens of longitudinal and transverse printed fiber directions.

For the specimen of longitudinal printing direction, the highest $\hat{\sigma}_{max}$ value was simulated for the model with the thinnest layer [Figure 11(a)]. This contradicts to experimental results where the specimen with layer height of 0.25 *mm* was strongest [Figure 11(b)]. The adhesion between the fibers in the same layer was poor for the samples with thin layers and did not fit the FE model of microstructure. However, experimental $\hat{\sigma}$ versus displacement curves for other groups were arranged in the same order as the curves obtained from the numerical simulations in the analyzed range.

The numerical simulations stopped because of failure to find equilibrium, and it was assumed that the models reach their maximum values before the instabilities occur. Similarly to the tension results, the experimental and simulated deflection values at which $\hat{\sigma}_{max}$ is reached differ less than 10 per cent for all models with the exception of the model corresponding to the layer height of 0.2 *mm*. Although the $\hat{\sigma}_{max}$ values differ less than 10 per cent for the models corresponding to the layer heights 0.35 *mm* and 0.4 *mm*, it is obvious that the numerical models tend to be weaker approximately by 20-33 per cent than the experimental specimens at the deflection 2 *mm* and by 22-32 per cent at the deflection 4 *mm*.

The bending zone of flexure test samples with layer thickness of 0.25 *mm* and 0.4 *mm* and longitudinal printing direction after the test are shown in Figure 12.

Figure 11 Typical $\hat{\sigma}$ versus deflection curves of numerical simulations (a) and experiments (b) of flexure test for specimen with longitudinal printing direction with $\hat{\sigma}_{max}$ values marked for each curve

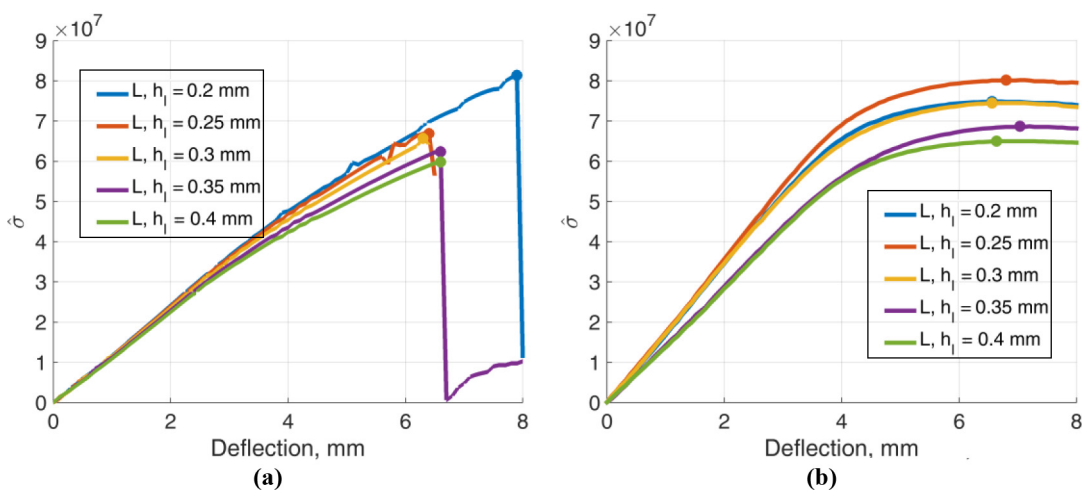

Figure 12 Bending zone of specimens with layer thickness 0.25 *mm* (a) and 0.4 *mm* (b) for longitudinal printing fibers after the flexure test

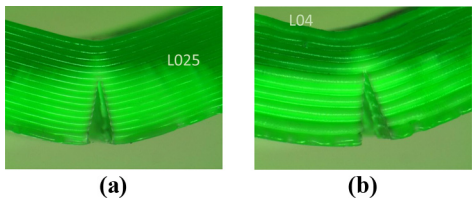

In case of group of specimens with transverse printing direction, the tendency that $\hat{\sigma}_{max}$ value is higher for the specimen with thinner layer was sustained in numerical simulation [Figure 13(a)]. This agrees with the experimental results [Figure 13(b)] although the experimental results for specimen with layers of 0.2 and 0.25 *mm* height differed insignificantly. However, the $\hat{\sigma}_{max}$ and extension values differ approximately 20 per cent for the numerical and experimental results. The numerical models tend to be weaker approximately by 19-30 per cent than the experimental specimens at the deflection 2 *mm* and by 19-25 per cent at the deflection 4 *mm*. The bending zone of flexure test samples with layer thickness 0.2 and 0.4 *mm* and transverse printing direction after the test are shown in Figure 14.

Although the simulation results showed that the $\hat{\sigma}_{max}$ value of model increases if the structure is manufactured with thinner layer, this contradicts to the experimental results implying that the strongest structure is printed with the layer height of 0.25 *mm*, while the 0.2 *mm* layer thickness performed best in numerical simulation. The limitation for the layer of 0.2 *mm* can be created by imprecisions of the printer and the fact that fused material is not spread widely enough to assure the adhesion between parallel roads in the same layer. The $\overline{\sigma}_{max}$ values of the samples differed less than 10 per cent from the mean values for both pattern types in the flexure test with the exception of the samples with the layer thickness 0.4 *mm*. This was a result of poor adhesion in the intersection areas.

On the contrary to the tensile test, the flexure test is governed by a combination of stresses and is strongly influenced by

Figure 14 Bending zone of specimens with layer thickness 0.2 *mm* (a) and 0.4 *mm* (b) for transverse printing fibers after the flexure test

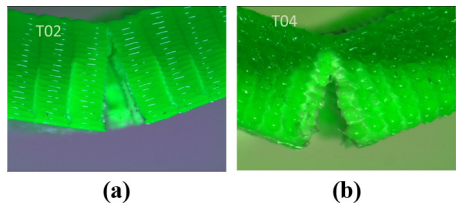

overlaps between the layers. The inter-layer intersection was not included in the RVE model and this resulted in a greater difference between the numerical and experimental results compared to the tensile test.

Furthermore, the models with parameters calculated for samples with longitudinal fibers gained higher $\hat{\sigma}_{max}$ values and were weakened at higher deflection values than the models with parameters calculated according samples with transverse fibers. Moreover, numerical simulations failed to find equilibrium for most of the models because of instabilities that are the result of steep fall of the input curves of the material model.

5. Conclusions

Three-dimensional printed items designated for real usage or operation have to support real loads; therefore, their mechanical strength should be estimated during the design stage. The length scales of the extruded fibers and the 3D printed item are significantly different. Therefore, direct 3D FE model representation of the item at micro level together with straightforward FEM/Experimental comparison was not possible because of the limitation of computational resources. Instead, the multi-scale FEM approach was applied. First, FE micro-scale model was analyzed to obtain effective stiffness tensor and stress–strain relationships of the equivalent orthotropic material. The close-to-reality geometry of five FE micro-scale models representing unidirectional 3DPIs with different layer thicknesses was developed on the basis of the

Figure 13 Typical $\hat{\sigma}$ versus deflection curves of numerical simulations (a) and experiments (b) of flexure test for specimen with transverse printing direction $\hat{\sigma}_{max}$ values marked for each curve

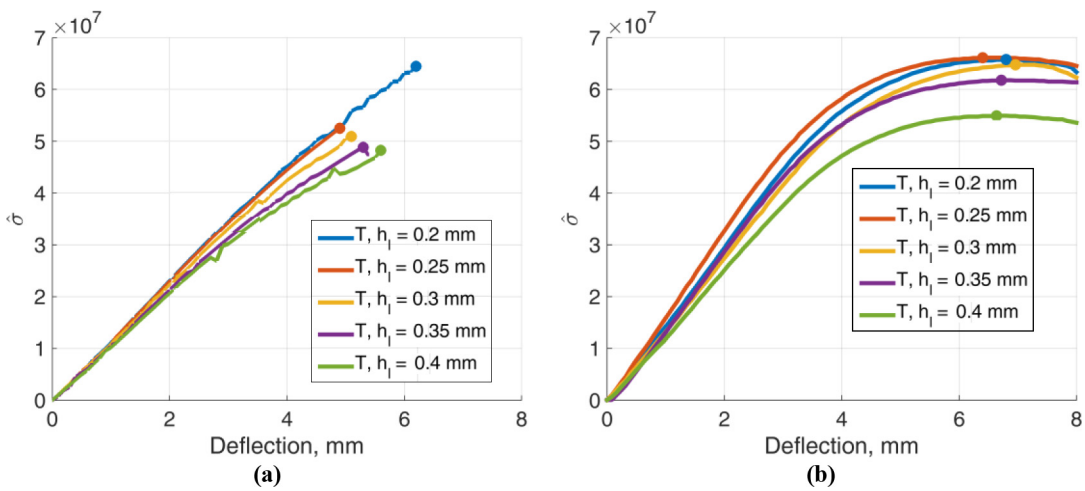

G-code. Each type of the extruded fiber pattern was characterized by the individual stiffness tensor and a set of stress–strain relationship curves. Second, the obtained parameters and relationships were used for creation of the FE model of the 3DPI in the macro-scale. LS-DYNA was used for micro- as well as, macro-scale simulations. However, the transition between the two scales is not automatic and must be properly designed. The main contribution of this article was to present the transition between two scales that would allow properly simulate non-linear behavior of the macro-scale model.

In the range of modest values of additive layer thicknesses and extruded fiber thicknesses, we succeeded to adjust the model parameters and to validate the values of stiffness and failure limits of the equivalent orthotropic material, which enabled to adequately simulate and predict the mechanical behavior of 3DPI samples in linear and non-linear stages of the response. However, certain difficulties remain in cases where the values of thicknesses are at the edge of the range specific to the 3DP used for our experiments. The inadequacies of numerical and experimental results also might have appeared because of inaccurate material parameters that are used in the computational micro-models of representative volume elements. Although the material properties of the fiber are approximately known, the properties at overlaps of adjacent fiber differ and should be included in the model. The experiments demonstrated that the influence of overlaps was strongly expressed in cases of thinnest and thickest layers.

A close-to-reality principal explanation of certain inadequacies between theory and experiment could be provided. FE models in both micro- and macro-scales were assumed to be "ideal". This means possible defects in the first printed additive layer could cause certain magnitudes of shear strains observed experimentally, however not implemented in numerical models. In addition, the RVE is analyzed with the assumption that it is always surrounded by other elements. This approach is incorrect for the elements near the surfaces of the macro-model. To represent stress–strain relations of these elements, the RVE should be analyzed with boundary conditions of prescribed displacements on one surface. Further on, real thermal effects may presumably cause a mismatch between the actual filling and the filling predicted by the programmed G-code. The mismatch might be avoided by introducing appropriate stiffness correction coefficients, which might be found by comparing computed and experimental results. The mismatch of filling patterns in experimental and numerical models might be reduced by revising material directions of each element according the G-code. Moreover, the actual precision of the printing hardware was not estimated. This motivates to further improve the current multi-scale modeling approach by including these factors.

References

Ahn, S.H., Montero, M., Odell, D., Roundy, S. and Wright, P.K. (2002), "Anisotropic material properties of fused deposition modeling ABS", *Rapid Prototyping Journal*, Vol. 8 No. 4, pp. 248-257.

Arivazhagan, A. and Masood, S.H (2012), "Dynamic mechanical properties of ABS material processed by fused deposition modelling", *International Journal of Engineering Research and Applications (IJERA)*, Vol. 2 No. 3, pp. 2009-2014, available at: www.ijera.com/papers/Vol2_issue3/LZ2320092014.pdf

Atzeni, E., Luliano, L., Minetola, P. and Salmi, A. (2010), "Redesign and cost estimation of rapid manufactured plastic parts", *Rapid Prototyping Journal*, Vol. 16 No. 5, pp. 308-317, available at: www.emeraldinsight.com/doi/abs/10.1108/13552541011065704

Bellini, A. and Güçeri, S. (2003), "Mechanical characterization of parts fabricated using fused deposition modeling", *Rapid Prototyping Journal*, Vol. 9 No. 4, pp. 252-264.

Calneryte, D. and Barauskas, R. (2016), "Multi-scale evaluation of the linear elastic and failure parameters of the unidirectional laminated textiles with application to transverse impact simulation", *Composite Structures*, Vol. 142, pp. 325-334, available at: http://linkinghub.elsevier.com/retrieve/pii/S0263822316300162

Chaitanya, S.K., Reddy, K.M., Naga, S. and Harsha, S. (2015), "Vibration properties of 3D printed/rapid prototype parts", *International Journal of Innovative Research in Science, Engineering and Technology*, Vol. 4 No. 6, pp. 4602-4608, available at: http://doi.org/10.15680/IJIRSET.2015.0406087

Chang, D.Y. and Huang, B.H. (2011), "Studies on profile error and extruding aperture for the RP parts using the fused deposition modeling process", *The International Journal of Advanced Manufacturing Technology*, Vol. 53 Nos 9/12, pp. 1027-1037.

Domingo-Espin, M., Puigoriol-Forcada, J.M., Garcia-Granada, A.A., Lluma, J., Borros, S. and Reyes, G. (2015), "Mechanical property characterization and simulation of fused deposition modeling Polycarbonate parts", *Materials & Design*, Vol. 83, pp. 670-677, available at: http://linkinghub.elsevier.com/retrieve/pii/S0264127515004244

Gorski, F., Wichniarek, R. and Kuczko, W. (2014), "Influence of filling type on strength of parts manufactured by fused deposition modelling", *Journal of Machine Engineering*, Vol. 14, No. 3, pp. 113-125.

Groza, J.R. and Shackelford, J.F. (2010), *Materials Processing Handbook*, CRC Press, Boca Raton.

Holland, D., O'Donnell, G. and Bennett, G. (2010), "Open design and the RepRap project", *27th International Manufacturing Conference*, pp. 97-106, available at: http://hdl.handle.net/2262/41053

Jami, H., Masood, S. and Song, W. (2013), "Dynamic response of FDM made ABS parts in different part orientations", *Advanced Materials Research*, Vol. 748, pp. 291-294.

Jones, R., Haufe, P., Sells, E. and Iravani, P. (2011), "RepRap – the replicating rapid prototyper", *Robotica*, available at: http://dx.doi.org/10.1017/S026357471000069X

Kentzer, J., Koch, B., Thim, M., Jones, R.W. and Villumsen, E. (2011), "An open source hardware-based mechatronics project: the replicating rapid 3-D printer", *4th International Conference on Mechatronics*, pp. 1-8.

Lee, C.S., Kim, S.G., Kim, H.J. and Ahn, S.H. (2007), "Measurement of anisotropic compressive strength of rapid prototyping parts", *Journal of Materials Processing Technology*, Vols 187/188, pp. 627-630.

Melenka, G.W., Schofield, J.S., Dawson, M.R. and Carey, J.P. (2015), "Evaluation of dimensional accuracy and material

properties of the MakerBot 3D desktop printer", *Rapid Prototyping Journal*, Vol. 21 No. 5, pp. 618-627, available at: www.emeraldinsight.com/doi/10.1108/RPJ-09-2013-0093

Pearce, J.M., Blair, C.M., Laciak, K.J., Andrews, R., Nosrat, A. and Zelenika-Zovko, I. (2010), "3-D printing of open source appropriate technologies for self-directed sustainable development", *Journal of Sustainable Development*, Vol. 3 No. 4, pp. 17-29.

Rodríguez, J.F., Thomas, J.P. and Renaud, J.E. (2003), "Mechanical behavior of acrylonitrile butadiene styrene fused deposition materials modeling", *Rapid Prototyping Journal*, Vol. 9 No. 4, pp. 219-230.

Sood, A.K., Ohdar, R.K. and Mahapatra, S.S. (2012), "Experimental investigation and empirical modelling of FDM process for compressive strength improvement", *Journal of Advanced Research*, Vol. 3 No. 1, pp. 81-90, available at: http://linkinghub.elsevier.com/retrieve/pii/S209012321100066X

Sood, A.K., Ohdar, R.K. and Mahapatra, S.S. (2010), "Parametric appraisal of mechanical property of fused deposition modelling processed parts", *Materials & Design*, Vol. 31 No. 1, pp. 287-295, available at: http://linkinghub.elsevier.com/retrieve/pii/S0261306909002945

Su, R., Campbell, G.M. and Boyd, S.K. (2007), "Establishment of an architecture-specific experimental validation approach for finite element modeling of bone by rapid prototyping and high resolution computed tomography", *Medical Engineering and Physics*, Vol. 29 No. 4, pp. 480-490.

Thrimurthulu, K., Pandey, P.M. and Venkata Reddy, N. (2004), "Optimum part deposition orientation in fused deposition modeling", *International Journal of Machine Tools and Manufacture*, Vol. 44 No. 6, pp. 585-594, available at: http://linkinghub.elsevier.com/retrieve/pii/S0890695503003262

Tymrak, B.M., Kreiger, M. and Pearce, J.M. (2014), "Mechanical properties of components fabricated with open-source 3-D printers under realistic environmental conditions", *Materials and Design*, Vol. 58, pp. 242-246, available at: http://dx.doi.org/10.1016/j.matdes.2014.02.038

Wittbrodt, B. and Pearce, J.M. (2015), "The effects of PLA color on material properties of 3-D printed components", *Additive Manufacturing*, Vol. 8, pp. 110-116, available at: http://linkinghub.elsevier.com/retrieve/pii/S2214860415000494

Corresponding author

Dalia Calneryte can be contacted at: dalia.calneryte@ktu.lt